

# Biochemical sensing with a polymer-based micromachined Fabry-Perot sensor

Tianhua Zhang<sup>1</sup>, Shantan Talla<sup>1</sup>, Zhongcheng Gong<sup>1</sup>, Sukrut Karandikar<sup>1,2</sup>,  
Rebecca Giorno<sup>2</sup>, and Long Que<sup>1,\*</sup>

<sup>1</sup>Institute for Micromanufacturing, Louisiana Tech University, Ruston, LA 71272, USA

<sup>2</sup>School of Biological Sciences, Louisiana Tech University, Ruston, LA 71272, USA

\*lque@latech.edu

**Abstract:** A white-light source operated polymer-based micromachined Fabry-Perot biochemical sensor is reported. As a refractive-index sensitive optical sensor, its transducing signal varies upon the changes of the effective refractive index in the Fabry-Perot cavity. This sensor is fabricated from PDMS and glass. More specifically, this sensor is a micromachined Fabry-Perot interferometer ( $\mu$ FPI) and is fabricated by bonding a glass substrate and the soft-lithographically patterned PDMS. Several biochemicals have been detected with the  $\mu$ FPI biochemical sensors. Measurements show that rabbit IgG at a concentration of as low as 5 to 50 ng/ml can be detected even without any performance optimization of the devices.

©2010 Optical Society of America

**OCIS codes:** (130.6010) Sensors; (050.2230) Fabry-Perot; (230.3990) Micro-optical devices.

---

## References and links

1. Z. D. Popovic, R. A. Sprague, and G. A. Connell, "Technique for monolithic fabrication of microlens arrays," *Appl. Opt.* **27**(7), 1281–1284 (1988).
2. C. H. Lee, H. Yoshida, Y. Miura, A. Fujii, and M. Ozaki, "Fabrication of micro-grating structures by direct laser writing based on two photon process and their liquid crystal alignment abilities," *IEICE Transactions on Electronics*, **E 91-C**(10), 1581–1586 (2008).
3. L. Hornbeck, "Deformable-mirror spatial light modulators," *Proc. SPIE, Spatial Light Modulators and Applications III*, v.**1150**, 86–102 (1990)
4. Q. Xu, and M. Lipson, "All-optical logic based on silicon micro-ring resonators," *Opt. Express* **15**(3), 924–929 (2007).
5. C. Wang, B. Wherrett, and T. Harvey, "Fabrication and characterization of a 4x4 array of asymmetric Fabry-Perot reflection modulators," *Electron. Lett.* **30**(15), 1219–1220 (1994).
6. N. Hall, and F. Degertekin, "Integrated optical interferometric detection method for micromachined capacitive acoustic transducers," *Appl. Phys. Lett.* **80**(20), 3859–3861 (2002).
7. J. Han, "Fabry-Perot cavity chemical sensors by silicon micromachining techniques," *Appl. Phys. Lett.* **74**(3), 445–447 (1999).
8. L. Que, "Two-dimensional tunable filter array for a matrix of integrated fiber optic input-output light channels", US Patent 6,449,410 (2002)
9. M. Blomberg, O. Rusanen, and K. Keranen, "A silicon microsystem-miniaturized infrared spectrometer," *Proc. 9th Int. Conf. On Solid-state Sensors, Actuators and Microsystems*, 1257–1258 (1997)
10. N. Neumann, M. Ebermann, K. Hiller, and S. Kurth, "Tunable infrared detector with integrated micromachined Fabry-Perot filter," *Proceedings of the SPIE*, v. **6466**, 646606–12 (2007)
11. L. Que, A. Zribi, A. Banerjee, and D. Hays, "Raman system on a chip," US Patent 7,505,128 (2009)
12. T. Dohi, K. Matsumoto, and I. Shimoyama, "The optical blood test device with the micro Fabry-Perot interferometer", *Proceedings of IEEE MEMS*, 403–406 (2004)
13. T. Dohi, K. Matsumoto, and I. Shimoyama, "The micro Fabry-Perot interferometer for the spectral endoscope", *Proceedings of IEEE MEMS*, 830–833 (2005)
14. K. M. van Delft, J. C. Eijkel, D. Mijatovic, T. S. Druzhinina, H. Rathgen, N. R. Tas, A. van den Berg, and F. Mugele, "Micromachined Fabry-Pérot interferometer with embedded nanochannels for nanoscale fluid dynamics," *Nano Lett.* **7**(2), 345–350 (2007).
15. Y. Zhang, H. Shih, K. L. Cooper, and A. Wang, "Miniature fiber-optic multicavity Fabry-Perot interferometric biosensor," *Opt. Lett.* **30**(9), 1021–1023 (2005).
16. J. Liu, Y. Sun, and X. Fan, "Highly versatile fiber-based optical Fabry-Pérot gas sensor," *Opt. Express* **17**(4), 2731–2738 (2009).
17. M. Born, and E. Wolf, *Principals of Optics* (John Wiley & Sons, Inc., 2000)
18. S. Jiang, B. Zeng, Y. Liang, and B. Li, "Optical fiber sensor for tensile and compressive strain measurement by white-light Fabry-Perot interferometry," *Opt. Eng.* **46**(3), 034402 (2007).

19. T. Zhang, Z. Gong, and L. Que, "A white-light source operated polymer-based micromachined Fabry-Perot chemo/biosensor," *Proc. of IEEE Intl. Conf. on NEMS*, 177–180 (2009)
20. S. Zangooi, R. Bjorklund, and H. Arwin, "Protein adsorption in thermally oxidized porous silicon layers," *Thin Solid Films* **313–314**(1-2), 825–830 (1998).
21. T. Zhang, Z. Gong, R. Giorno, and L. Que, "Signal sensitivity and intensity enhancement for a polymer-based Fabry-Perot interferometer with embedded nanostructures in its cavity," *Proceeding of 15th International Conference on Solid-State Sensors, Actuators & Microsystems (Transducers'09)*, 2310–2313 (2009)
22. J. Zhao, X. Zhang, C. R. Yonzon, A. J. Haes, and R. P. Van Duyne, "Localized surface plasmon resonance biosensors," *Nanomedicine (Lond)* **1**(2), 219–228 (2006).

## 1. Introduction

The utilization of an optical technique for sensing applications offers some attractive features over other techniques such as high degree of sensitivity, capability of multiplexing and immunity to environment noise. With the advancement of micro and nanofabrication technologies, many optical components or systems such as lenses, gratings, mirrors, micro ring resonators and interferometers have been miniaturized [1–5]. As a result, the field of microoptics and nanooptics has emerged, triggering extensive research to scale down the optics-based sensing platforms for the past decades. One example is the miniaturization of Fabry-Perot interferometers. Micromachined Fabry-Perot interferometers ( $\mu$ FPIs) or optical fiber based miniature FPIs have been designed and implemented for chemical sensing, gas sensing, biosensing, ultrasonic sensing and optical modulation [5–16]. For chemical and gas sensing, the output signals are transmitted intensity of light through FPI, which vary with different chemicals or gases inside the FPI cavity [7–9]. For ultrasonic sensing, the micromachined capacitive acoustic transducer consists of a FPI cavity with embedded optical diffraction gratings. Optimization of the detection sensitivity can be achieved by deflecting the membrane of the FPI [6]. For optical modulation, a FPI contains a crosslinked electro-optic polymer inside its cavity, offering the potential for high time-bandwidth modulation [5].  $\mu$ FPI has also been utilized for studying the nanoscale fluidic dynamics [14], indicating its potential for nanoscience and nanotechnology research. Use of MEMS actuation technology, tunable  $\mu$ FPIs have been designed and implemented successfully, which have significantly expanded and enriched the applications of FPIs. Specifically, tunable  $\mu$ FPIs have been developed for wavelength division multiplexing (WDM) in optical communications [8] and Raman spectroscopy [11], oxygen detection in blood samples [12] and spectral endoscope optical imaging [13]. For WDM applications, a tunable  $\mu$ FPI is used as a tunable filter, selecting different wavelengths by changing the FPI cavity length. For oxygen detection in blood samples, the tunable  $\mu$ FPI device is used for a broad wavelength range from visible to near infrared light, offering sufficient characteristics to analyze the spectrum of the blood. For spectral endoscope optical imaging, the tunable device is used for acquisition of spectral images of a target at each pixel. The structural materials for most of the reported  $\mu$ FPIs, which are mainly operated using a laser source, are silicon, polysilicon, silicon nitride, silicon oxide thin film or other semiconductor materials [5–14]. In this article, we report a polymer-based  $\mu$ FPI biochemical sensor operated with a white-light source.

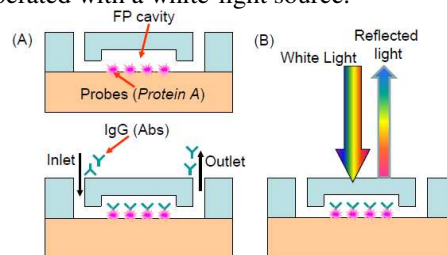


Fig. 1. (A) Schematic of a PDMS-based  $\mu$ FPI biochemical sensor, showing immobilized probes (Protein A) on the glass surface and the binding between Immunoglobulin G (IgG) antibodies and probes; (B) Operational principle of the  $\mu$ FPI: the reflected light from the  $\mu$ FPI as the output transducing optical signals

## 2. Operation principle of the device

Figure 1 shows the schematic and operational principle of a white-light source operated  $\mu$ FPI biochemical sensor. This sensor is micromachined from polydimethylsiloxane (PDMS) and glass. The  $\mu$ FPI cavity serves as the sensing region with a gap size of 50  $\mu\text{m}$ . Different from a traditional macroscale FPI or other reported  $\mu$ FPIs, neither of the FPI plates has been coated with any thin films for the enhancement of their reflectivity. The operation principle of this sensor is described as the following: Upon entering the FPI cavity, the operation light undergoes multiple internal reflections between the two FPI plates and interferences inside the cavity. As a result, modulated output transducing signals such as reflected interference fringes are generated as show in Fig. 1(B) and Fig. 2(A). More specifically, Protein A molecules serve as the probes and are immobilized on one FPI plate surface (Fig. 1(A)). When a variety of Immunoglobulin G (IgG) antibodies are flown through the cavity, they bind to the Protein A, causing changes of the effective index of refraction, resulting in the interference fringes shift ( $\Delta\lambda$ ) (Fig. 2(A)), which serves as the optical transducing signals.

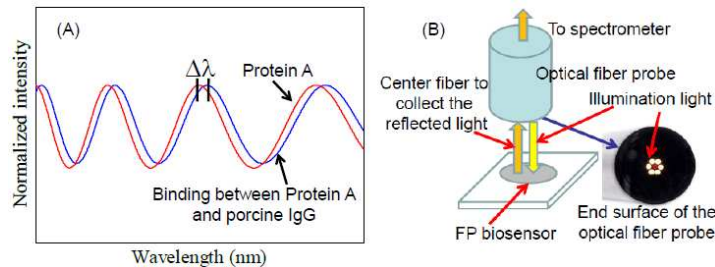


Fig. 2. (A) A sketch showing the inference fringe shift ( $\Delta\lambda$ ) due to the effective index of refraction changes in the FPI cavity with the binding between Protein A and porcine IgG; (B) Testing setup: a custom-designed optical fiber probe (Ocean Optics, Inc) consists of a tight bundle of 7 optical fibers in a stainless steel ferrule. The center fiber is to collect the reflected light while the outer 6 fibers deliver illumination light to the biochemical sensor

Figure 2(B) gives the sketch of the testing setup for the  $\mu$ FPI biochemical sensor. A custom-designed optical fiber probe (Ocean Optics, Inc.) delivers white light from a tungsten halogen source (Ocean Optics, Inc.) perpendicularly to a biochemical sensor. This probe also receives the reflected signals from the sensor, which is eventually coupled to a HR4000 Spectrometer (Ocean Optics, Inc.).

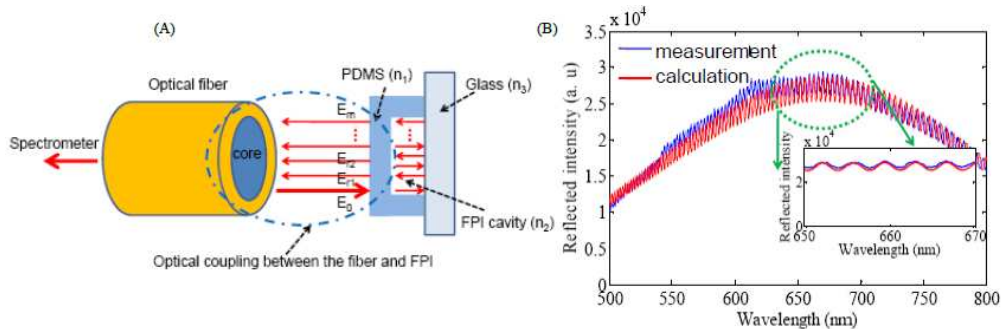


Fig. 3. (A) Sketch of the optical system including the optical fibers and the  $\mu$ FPI device: the indexes of refraction of PDMS, medium in FPI cavity and glass are  $n_1$ ,  $n_2$  and  $n_3$ ; (B) Based on Eq. (1) and (2), the calculated matches the measured transducing optical signals from the biochemical sensor

## 3. Device design, modeling and fabrication

Figure 3 shows the sketch of the optical system consisting of an optical fiber and a  $\mu$ FPI for the modeling. The white light delivered from the optical fiber to the sensor can be modeled as

a Gaussian beam [17–19]. Due to the fiber core finite size of the optical fiber probe, the loss of the optical coupling between the fiber and  $\mu$ FPI sensor needs to be considered.

Assume the optical power loss coefficient of  $\mu$ FPI cavity is  $L_{FPI}$  and the coupling loss between the fiber probe and  $\mu$ FPI is  $L_{fiber-FPI}$ , then the reflected intensity  $I_r$  from this system, coupled to the spectrometer, is written as:

$$I_r = I_i \exp\left(-\frac{2(\lambda - \lambda_0)^2}{\omega^2}\right) \times L_{fiber-FPI} \times f(R_{air-PDMS}, R_{air-glass}) \quad (1)$$

Where

$$f(R_{air-PDMS}, R_{air-glass}) = \frac{r_2^2 + r_3^2 L_{FPI}^2 - 2r_2 r_3 L_{FPI} \cos(2kn_2 d)}{1 - r_2^2 r_3^2 L_{FPI}^2 - 2r_2 r_3 L_{FPI} \cos(2kn_2 d)} \quad (2)$$

and

$$r_2 = -r_1 = \frac{n_2 - n_1}{n_2 + n_1}, \quad r_3 = \frac{n_2 - n_3}{n_2 + n_3}$$

Where  $I_i \exp(-2(\lambda - \lambda_0)^2/\omega^2)$  is incident light intensity;  $\lambda_0$  is the center wavelength of the light source,  $\omega$  is the beam radius at the beam waist;  $f(R_{air-PDMS}, R_{air-glass})$  is the reflectivity from the  $\mu$ FPI;  $R_{air-PDMS}$ ,  $R_{air-glass}$  are the reflectivity at the interface between the air and PDMS, the air and glass, respectively and  $d$  is the gap size of FPI cavity;  $n_1$ ,  $n_2$  and  $n_3$  are the indices of refraction of PDMS, medium in FPI cavity and glass, respectively.

The fabrication process flow of the devices utilizing an inexpensive and rapid soft lithography process is shown in Fig. 4 (A). Briefly, using conventional optical lithography a 50  $\mu$ m thick SU8 mold of the device is fabricated on a silicon substrate. PDMS is then casted on the mold, followed by 1.5 hour curing at the temperature of 65 °C. The patterned PDMS layer and the glass substrate are bonded together after oxygen plasma treatment, followed by the formation of the input and output wells in the PDMS layer. Optical micrographs of SU8 molds, fabricated PDMS devices and assembled devices with tubing are given in Fig. 4(B-F). Note that the arrayed devices can be readily and rapidly batch-fabricated, offering a cost-effective and disposable biosensing technical platform with high throughput.

As an example for the validation of the optical model described above, the measurement of the output signals from a  $\mu$ FPI device with air inside its cavity has been performed. The calculated signals with air in the FPI cavity match the measured signals very well as shown in Fig. 3 (B). The intensity profile offset of the calculated results from the measured results is mainly due to the fact that the light source is not an ideal Gaussian beam.

#### 4. Experimental results and discussions

A protein-protein binding assay has been used to demonstrate the operation and biomolecular detection capability of the polymer-based  $\mu$ FPI at room temperature. The detailed experimental materials and procedure are described in the following.

The assay reagents used in the experiments include Protein A (Pierce Biotechnology), buffer solution phosphate buffered saline (PBS) (Sigma-Aldrich), Sea Block (Pierce Biotechnology), and porcine, rabbit, or sheep immunoglobulin G (IgG) (Sigma-Aldrich).

Specifically, Protein A is prepared in PBS solution at a concentration of 500  $\mu$ g/ml, which can be diluted accordingly for different concentrations. The blocking buffer, Sea Block, used to minimize the non-specific binding is mixed with PBS solution with a ratio of 1:4. Similarly, the porcine, rabbit, sheep IgG anti-sera are diluted with PBS to achieve final concentrations of 500  $\mu$ g/ml, 500 ng/ml, 50 ng/ml, and 5 ng/ml, for each species respectively.

As a reference, the first measurement is taken with air inside the FPI cavity. The PBS solution is flowed into the cavity with a flow rate of 0.5  $\mu$ l/minute the slowest possible flow rate to avoid any deformation of the PDMS plate of the FPI. In addition, care is taken to eliminate any air bubbles inside the cavity throughout the experiment. The measurement is

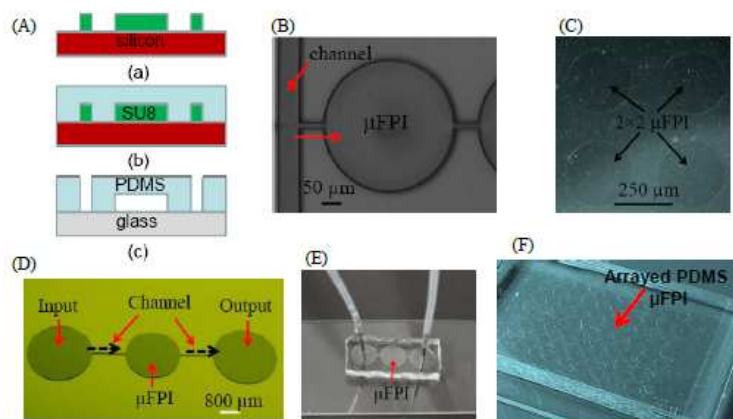


Fig. 4. (A) The fabrication process flow: (a) form the 50 $\mu\text{m}$  tall SU8 mold on the silicon wafer; (b) transfer the mold to PDMS; (c) bond patterned PDMS to glass wafer after plasma treatment, and then form the input /output wells; (B) Optical micrograph of SU8 mold for a PDMS-FPI with integrated microfluidic channel to deliver chemicals to the FPI cavity; (C) Optical micrograph of  $2 \times 2$  PDMS-FPIs; (D-E) Photos of one SU8 mold and one assembled PDMS-FPI biochemical sensor; (F) A photo of arrayed PDMS-FPI biochemical sensors

taken with PBS solution, which is used to calibrate the cavity gap based on the measured index of refraction of PBS being 1.336 [20]. Thereafter, the Protein A solution (500 $\mu\text{g}/\text{ml}$ ) is slowly passed into the device with flow rate of 0.5 $\mu\text{l}/\text{minute}$  and allowed to stay inside the FPI cavity for 30 minutes at room temperature. This will allow the Protein A to bind to the glass surface and serve as probes. The unbound Protein A is washed away using PBS solution. The washing routine is done for at least 3 cycles of 3 minutes each. The measurement is taken at each interval and checked for measurement repeatability. The Sea Block solution is passed into the device with the same flow rate to block the unmodified or unbound sites in the FPI cavity. The Sea Block solution is allowed to stay inside FPI cavity for 15 minutes at room temperature. After the specified time the Sea block solution is pumped out and the wash routine is performed again to take some measurements. Similarly the rabbit IgG solution made with PBS solution is passed into the device and allowed it settle for 15 to 30 minutes in the FPI cavity at room temperature. The measurements are taken at regular intervals after washing the excess unbound rabbit IgG using PBS solution. Similarly the same procedure is repeated with porcine and sheep IgGs for different concentrations and measurements are carried out. Note that all the measurements are performed after the fluidic channel has become dried.

As examples, the measured transducing signals for PBS, immobilized Protein A, Protein A bound with porcine IgG and Protein A bound with rabbit IgG are shown in Fig. 5(A-B). The shift in interference fringes is clearly observed. In Fig. 5(C), the transducing signals of Protein A and its binding with porcine, sheep and rabbit IgGs are plotted together. Again the fringe shift is clearly visible, indicating the difference of the effective of refraction indices of these three different types of IgGs. In Table 1, the average fringe peak shifts relative to the air inside the FPI cavity for different cases are summarized. The average shift for each case is obtained by averaging the shift of the fringe peaks between the 600 nm –720 nm spectrum window. The fringe peaks are identified based on the fitting curves using the proposed mathematical model, which also facilitates the determination of the peak shift larger than free spectral range (FSR), which is around 3–4 nm for this  $\mu\text{FPI}$  device. Measurement error is  $\pm 0.01$  nm due to the resolution of the HR4000 Spectrometer is 0.02 nm. Note that the concentrations of Protein A, porcine, rabbit and sheep IgGs are all 500  $\mu\text{g}/\text{ml}$ . Use of the index of refraction of PBS 1.336, the FPI cavity length is calculated to be 48  $\mu\text{m}$ , which is 2  $\mu\text{m}$  offset from the nominal length of the design. This reduction of the cavity length is

probably due to the thickness change of the SU8 mold during the microfabrication process. Based on the FPI cavity calibration with PBS solution, using similar calculation method, the effective refractive indices of Protein A and Protein A bound with rabbit IgG at concentration of 50 ng/ml are 1.521 and 1.550, respectively. Note that the effective refractive indices for Protein A bound with different types of IgG or the same IgG but at varied concentrations are different.

In Table 2, the fringe shift for rabbit IgG with varied concentrations is summarized. The higher the concentration of the rabbit IgG, the more binding between Protein A and rabbit IgG occurs, resulting in higher effective index of refraction changes thus bigger effective optical thickness (EOT) changes inside the FPI cavity. Hence a greater shift of the fringe peaks is achieved. In other words, as the concentration of rabbit IgG decreases, the shift also decreases. It is observed that when the concentration of rabbit IgG is reduced to 5 ng/ml, the fringe shift relative to the air inside the FP cavity is 0.68 nm, the same as that (0.69 nm) of Protein A without binding to rabbit IgG, suggesting the possible detection limit (DL) to be between 50 ng/ml and 5 ng/ml for this FPI biochemical sensor before optimization.

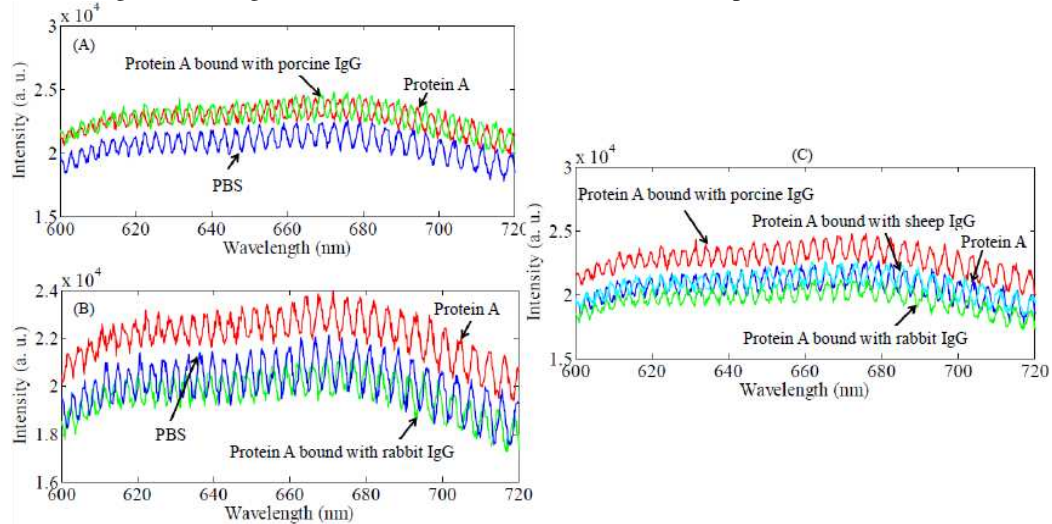


Fig. 5. (A-B) Measured signals for PBS, immobilized Protein A (500  $\mu\text{g/ml}$ ), Protein A bound with porcine IgG (500  $\mu\text{g/ml}$ ) and protein A bound with rabbit IgG (500  $\mu\text{g/ml}$ ); (C) Measured transducing signals for immobilized Protein A (500  $\mu\text{g/ml}$ ), Protein A bound with porcine IgG (500  $\mu\text{g/ml}$ ), rabbit IgG (500  $\mu\text{g/ml}$ ) and sheep IgG (500  $\mu\text{g/ml}$ ) respectively, showing clear shift of the interference fringes

**Table 1. Fringe peak shift relative to air for Protein A and different IgG samples**

Material	Average interference peak shift relative to air (600 nm-720 nm)
Protein A (500 $\mu\text{g/ml}$ )	$0.69 \pm 0.01$ nm
Protein A with Sea Block	$0.68 \pm 0.01$ nm (basically no shift compare to Protein A)
Protein A bound with porcine IgG (500 $\mu\text{g/ml}$ )	$4.56 \pm 0.01$ nm
Protein A bound with rabbit IgG (500 $\mu\text{g/ml}$ )	$3.67 \pm 0.01$ nm
Protein A bound with sheep IgG (500 $\mu\text{g/ml}$ )	$1.04 \pm 0.01$ nm

**Table 2. Fringe peak shift relative to air for rabbit IgG samples with varied concentrations**

Material	Average interference peak shift relative to air (600 nm-720 nm)
Protein A (500 $\mu\text{g/ml}$ )	$0.69 \pm 0.01$ nm
Protein A bound with rabbit IgG (500 $\mu\text{g/ml}$ )	$3.67 \pm 0.01$ nm
Protein A bound with rabbit IgG (500 ng/ml)	$1.29 \pm 0.01$ nm
Protein A bound with rabbit IgG (50 ng/ml)	$1.09 \pm 0.01$ nm
Protein A bound with rabbit IgG (5 ng/ml)	$0.68 \pm 0.01$ nm

## **5. Conclusion**

In summary, a polymer-based micromachined FPI biochemical sensor has been developed and its biomolecular detection capability has been demonstrated successfully. The simple, cost-effective and disposable nature of this type of sensor is attractive for point-of-care biodetection applications. The experiments show that detection limit (DL) of this sensor is between 50 and 5 ng/ml for the rabbit IgG. It is highly possible to enhance the sensitivity and DL significantly by introducing some nanostructures inside the FPI cavity [21,22].

## **Acknowledgement**

This research is supported in part by grants of NSF CAREER Award 2009 and NSF 2008 PFUND-110. The authors thank the technical support from the technical staffs at Institute for Micromanufacturing at Louisiana Tech University